Nanoscale

ROYAL SOCIETY OF CHEMISTRY

PAPER

View Article Online
View Journal | View Issue

Check for updates

Cite this: *Nanoscale*, 2024, **16**, 21837

Photoemission spectroscopy and microscopy for $Ta@Si_{16}$ superatoms and their assembled layers†

Masahiro Shibuta, ‡[a] Tsutomu Ohta,[b] Toshiaki Kamoshida,[b] Kana Yamagiwa,[b] Hironori Tsunoyama,[b] Tomoya Inoue,[b] Tsugunosuke Masubuchi [b] and Atsushi Nakajima *[a,b]

Received 5th July 2024,
Accepted 27th October 2024

DOI: 10.1039/d4nr02778g

rsc.li/nanoscale

Superatoms (SAs) with specific compositions have the potential to significantly advance the field of nanomaterials science, leading to next-generation nanoscale functionalities. In this study, we fabricated assembled layers with tantalum metal-atom encapsulating silicon cage ($Ta@Si_{16}$) SAs on an organic C_{60} substrate through deposition, and we characterized their electronic and optical properties by photoelectron spectroscopy and microscopy. The alkaline nature of $Ta@Si_{16}$ SAs reveals their electronic behaviors, such as charge transfer and electromagnetic near-field sensing, through two-photon photoemission (2PPE) spectroscopy and microscopy with a femtosecond laser. The evolution of the work function for $Ta@Si_{16}$ SAs on C_{60}, observed by 2PPE spectroscopy, demonstrates charge transfer complexation between the topmost C_{60} layer and the first $Ta@Si_{16}$ layer, consistent with the electron-donating alkaline characteristics of $Ta@Si_{16}$ SAs. Specifically, a small amount of $Ta@Si_{16}$ SA deposition leads to a dramatic increase in 2PPE intensity, attributable to electromagnetic near-field enhancements, suggesting applications as sensitizers for nonlinear imaging in photoemission microscopy. For the assembled $Ta@Si_{16}$ SA layers, a plasmonic response of $h\nu_p = 17.9$ eV is spectroscopically identified, including their valence and conduction band structures, and the plasmonic energetics are discussed in the context of metal doping in bulk silicon.

1. Introduction

Nanoclusters (NCs) with countable numbers of atoms are promising functional materials for future electronic and optical devices. Among the vast combinations of atomic species and their numbers, stably existing NCs with specific atomic compositions have been identified as "superatoms" (SAs),[1–8] whose characteristic stabilities are governed by geometric and electronic factors. Following the discovery of fullerenes as SAs,[9] extensive research has been conducted on $X@Al_{12}$ (X = B and Al)[10–13] and metal-encapsulating silicon cage ($M@Si_{16}$) SAs[14–21] in the gas phase, leading to the exploration of ligated metal NCs, such as $Au_n(SR)_m$,[22–26] in the liquid phase.

$M@Si_{16}$ SAs, in particular, are of potential interest as silicon-based nanomaterials, where their electronic properties can be tuned by endohedral doping of central metal atoms in a common Si caged structure (Fig. 1 inset). According to the 68-electron counting rule in SAs ($4e^- \times 16$ for the Si cage and ne^- for the central metal atom), $M@Si_{16}$ SAs with group 4 metals ($n = 4$; Ti, Zr, and Hf) exhibit electronically insulating properties due to electron shell closures, behaving as intrinsic semiconductors. By substituting the central metal with group 3, 5, and 6 metals ($n = 3$; Sc, Y, Lu, $n = 5$; V, Nb, Ta, and $n = 6$; Cr, Mo, W), they acquired n-type ($n = 3$) and p-type ($n = 5$ and 6) characteristics with a deficiency or surplus of electron(s).[14,17,20,21]

When non-ligated SAs generated in the gas phase are deposited on a substrate, a chemical interaction between the SAs and the substrate occurs, resulting in their favorable charge states.[27–36] The molecularly local electronic structure resulting from this interaction governs the charge injection/ejection properties at the hetero-interface. Furthermore, in films with deposited SAs, chemical interactions between neighbouring SAs provide additional functionalities, such as electric conduction and charge separation properties.[37,38] To further understand and control functional systems based on SAs, it is important to characterize the electronic and optical properties of SA layers/films grown on substrates.

---

[a] *Keio Institute of Pure and Applied Sciences (KiPAS), Keio University, 3-14-1 Hiyoshi, Kohoku-ku, Yokohama 223-8522, Japan. E-mail: nakajima@chem.keio.ac.jp; Fax: +81-45-566-1697; Tel: +81-45-566-1712*

[b] *Department of Chemistry, Faculty of Science and Technology, Keio University, 3-14-1 Hiyoshi, Kohoku-ku, Yokohama 223-8522, Japan*

† Electronic supplementary information (ESI) available: Notes S1 and S2, Fig. S1–S9, and Tables S1 and S2. See DOI: **https://doi.org/10.1039/d4nr02778g**

‡ Present address: Department of Physics and Electronics, Graduate School of Engineering, Osaka Metropolitan University, 1-1, Gakuen-cho, Naka-ku, Sakai, Osaka 599-8531, Japan.

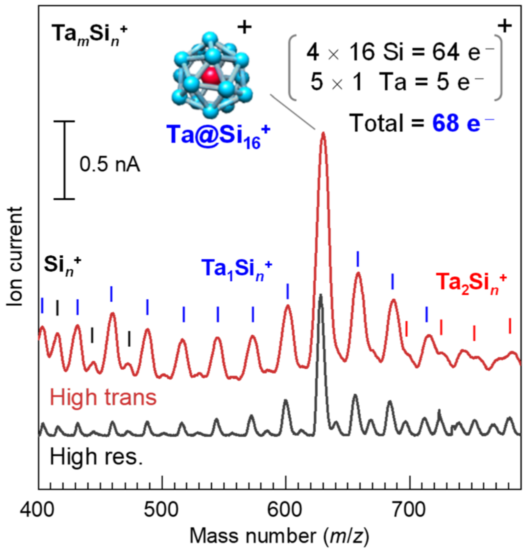

Fig. 1 Mass spectra of the $Ta_mSi_n^+$ binary nanocluster generated by an MSP source with different mass resolutions ($m/\Delta m$) of 100 (bottom) and 50 (top). The $Ta@Si_{16}$ superatoms (SAs) are selectively generated at m/z = 630 among the series of Si_n^+, $Ta_1Si_n^+$, and $Ta_2Si_n^+$ nanoclusters. With moderate mass resolution, SA deposition was size-selectively performed in high-transmission mode, fixed to the mass number of the $Ta@Si_{16}$ SA. The ion currents typically were several nA during deposition, corresponding to 6.2×10^9 SAs per nA per s. Since the $Ta@Si_{16}$ SA exhibits a p-type (alkaline-like) nature due to its one-electron excess, the cationic $Ta@Si_{16}^+$ SA satisfies the shell closure of 68 electrons.

Over the past decade, significant advancements have been made in the precise synthesis and deposition of atomically mass-selected NCs, including SAs,[27–36] where the deposited NCs/SAs on substrates have been characterized by conventional methods for materials science (*e.g.*, photoelectron spectroscopy,[27–36] scanning tunnelling microscopy (STM),[39,40] and X-ray absorption fine structure (EXAFS)).[41] Recent developments in size-selected NC deposition methodologies have addressed the abovementioned fundamental issues; the flux of an atomically mass-selected SA beam now allows for the fabrication of SA multilayers on substrates within a realistic timeframe (within several hours of operation), with a beam flux comparable to that of the molecular beam epitaxy (MBE) method used to form highly crystalline inorganic/organic epitaxial films.[42] The electronic conduction properties of size-selected SA films have been characterized, revealing their potential utility in functional nanodevices.[43,44]

In the initial stage of SA film growth on substrates, $M@Si_{16}$ SAs have been found to be stably immobilized on organic substrates by appropriately selecting their molecular properties (*e.g.* p- or n-type); positively or negatively charged SAs are stabilized with p- or n-type molecular characteristics, leading to molecularly favourable charge transfer interactions at their interfaces.[27–36] While pure $M@Si_{16}$ SA films have been shown to be tolerant to the ambient environment when protected by an overlayer,[42] the collective electronic/optical behaviors of assembled $M@Si_{16}$ SA layers remain uncharacterized beyond the nature of locally immobilized SAs.

In this study, we have characterized the electronic structures of p-type $Ta@Si_{16}$ SA layers grown on an organic n-type C_{60} fullerene substrate by detecting photoelectrons excited by different light sources. During the initial stage of depositing a small amount of $Ta@Si_{16}$ SAs (section 3.1), ranging from submonolayer to several monolayers (MLs), we focus on the interfacial characteristics of electronically excited states and changes in the work function (section 3.1.1),[45–49] using two-photon photoemission (2PPE) spectroscopy with a femtosecond light source. The quantitative evolution of the work function with increasing SA coverage (section 3.1.2) demonstrates the formation of an adsorption-induced surface dipole at the interface between the first layer of the p-type (or alkaline-like) $Ta@Si_{16}$ SA and the n-type C_{60} substrate due to charge transfer interactions. Furthermore, 2PPE spectroscopy resolves the photoexcited electrons in the conduction band of the $Ta@Si_{16}$ SA layer (section 3.1.3), while the 2PPE intensity is dramatically enhanced by the characteristic nonlinear optical responses of $Ta@Si_{16}$ SAs, indicating that the optical responses can be used as sensitizers for nonlinear microscopic imaging to visualize surface plasmon polariton (SPP) propagation at buried metal–dielectric interfaces (section 3.1.4). For thicker assembled $Ta@Si_{16}$ SA layers, with up to 7 MLs (section 3.2), we further characterized the chemical state and plasmonic response of the SA film by X-ray photoelectron spectroscopy (XPS) (section 3.2.1). The plasmon excitation of these SA layers, influenced by metal-atom encapsulation, differs from that of pure bulk Si crystals. Ultraviolet photoelectron spectroscopy (UPS) and 2PPE spectroscopy provide insights into electronic structures both below and above the Fermi level (E_F), with the experimental observations further supported by DFT calculations (section 3.2.2).

2. Experimental section

2.1. Fabrication of the $Ta@Si_{16}$ SA film on a C_{60} substrate

The $Ta@Si_{16}$ SA film was prepared using a magnetron sputtering (MSP) NC deposition method, with the detailed methodology described elsewhere.[29,30,50] In brief, Ta and Si atoms evaporated by Ar ion sputtering aggregate into NCs in cooled He gas. The charged NCs, including SAs, are introduced into a quadrupole mass filter using ion optics. Fig. 1 shows the mass spectra of the cationic Ta–Si binary NCs synthesised with the MSP source using a Ta–Si mixed target. The high-resolution mode spectrum (bottom spectrum) shows a prominent peak at m/z = 630, corresponding to the $Ta@Si_{16}$ SA, indicating its magic number behavior. The neighbouring product peaks, Si_{22} (m/z = 616) and Ta_2Si_{10} (m/z = 642), are well-separated from the $Ta@Si_{16}$ SA peak and are weak (a few %) compared to the dominant SA production. The targeted pure $Ta@Si_{16}$ SA can then be deposited in high-transmission mode (top spectrum), with an organic substrate placed at the throughput of a Q-mass filter, fixing the potentials of the electrodes in the mass filter for a specific mass number (m/z = 630 for the $Ta@Si_{16}$ SA). The flux of the SA beam is sufficient to reach several nA (6.2×10^9 SAs per nA per s) in the latest development, enabling the preparation of a 1 ML Ta@Si$_{16}$ SA film (corresponding to 5×10^{13} SAs; see ESI Note S1 and Fig. S1†) on a substrate within 1 hour of operation.

Since the Ta@Si$_{16}$ SA has p-type character (68 electron shell closure in a cationic state), an n-type organic substrate is plausible.[28,30,31–33] Here, we chose an n-type C$_{60}$ substrate, prepared by vacuum deposition on a graphite-based solid just before SA deposition. The C$_{60}$ thickness was 2 MLs, sufficient to electronically decouple the SA from the graphite. We also prepared a thick C$_{60}$ substrate (10 MLs) on a plasmonic gold (Au) (111) substrate, demonstrating the visualization of lateral plasmonic excitation[51–58] at the C$_{60}$/Au(111) interface sensitized by SA deposition (see section 3.1.4). The C$_{60}$ substrates were immediately transferred to the SA deposition system without disrupting the ultrahigh vacuum conditions.

2.2. Photoelectron spectroscopy and microscopy

The growth of the SA film and its electronic properties were evaluated using a photoelectron spectroscopy system (VG Scienta R-3000) with various photon sources, including XPS, UPS, and 2PPE. In XPS, an MgKα characteristic X-ray source (photon energy, $h\nu = 1253.6$ eV) was used to extract photoelectrons from the core levels of the atoms in the sample. We set the detection takeoff angle to 45° for surface sensitivity. The instrumental resolution, evaluated by the Au 4f$_{7/2}$ core level, was 1.12 eV, primarily governed by the intrinsic line width of the MgKα line.[59] The binding energy was calibrated to the energy of the Au 4f$_{7/2}$ peak at 84.0 eV.

For UPS, a He I discharge lamp ($h\nu = 21.22$ eV) was employed to observe the valence electronic structures with high energy resolution (<30 meV). In the case of 2PPE spectroscopy, the third harmonics of a titanium sapphire laser (COHERENT: Mira 900-F) were generated and focused onto the sample surface with an aluminium concave mirror ($f = 400$ mm). 2PPE can observe the unoccupied electronic states (or conduction bands) above the E_F with energy resolution comparable to that of UPS (30 meV).[60–62] Due to the surface sensitivity in the region of photoelectron kinetic energy being sufficient, normal emission of photoelectrons was detected in both UPS and 2PPE spectroscopy. Furthermore, 2PPE spectroscopy is valuable for evaluating the work function, as the detection area is limited with respect to the spot size of the incident laser (approximately 0.1 mm in diameter). To avoid unexpected effects of the local work function on surface defects or impurities, we selected the probe area for obtaining reproducible spectral data.

We also employed photoelectron emission microscopy (PEEM; IS-PEEM, FOCUS GmbH) to image the lateral distribution of 2PPE, *i.e.* 2P-PEEM. As mentioned in section 3.1.4, plasmonic excitation and propagation at the metal/dielectric interface can be visualized using 2P-PEEM,[51–58] where both fundamental and third harmonics of the titanium sapphire laser were irradiated onto the plasmonic sample with spatiotemporal overlap. The incident angle of the light source was 75° relative to the surface normal. The lateral resolution of the 2P-PEEM setup was better than 80 nm, depending on the extractor lens voltage of the PEEM optics.[48,63,64] In general, 2P-PEEM images of inhomogeneous samples show significant photoemission signals from defects or impurities. In our case, however, no such "hot spots" were observed, confirming the uniformity of the sample. This uniformity was ensured by performing all experimental procedures and measurements within the UHV system.

3. Results and discussion

3.1. 2PPE spectroscopy and microscopy for Ta@Si$_{16}$ SAs on C$_{60}$ organic surfaces

3.1.1. 2PPE spectra of Ta@Si$_{16}$ SA/C$_{60}$. Fig. 2(a) shows the 2PPE spectra for various coverages of Ta@Si$_{16}$ SAs on a C$_{60}$ substrate, where the nominal coverages were evaluated from the product amount of ion current × deposition time, as well as a step-by-step analysis of XPS measurements (ESI Note S1 and Fig. S1†). Incident photons of $h\nu = 4.13$ eV are used as both pump and probe photons in a one-color 2PPE manner. The lower horizontal axis represents the final state energy with respect to the E_F, while the top axis represents the intermediately excited state energy by one-photon absorption (final state energy minus $h\nu$). Before SA deposition (0 ML), the main two peaks observed are assignable to the lowest unoccupied molecular orbital (LUMO; $E_F + 0.8$ eV, see the upper axis) and LUMO+1 ($E_F + 1.8$ eV) of C$_{60}$ molecules.[61] The low-energy cutoff of the 2PPE spectrum, 4.71 eV in final state energy, corresponds to the vacuum level (E_{vac}) relative to the E_F, which is the work function ($=E_{vac} - E_F$) of a C$_{60}$ substrate.

Upon deposition of the Ta@Si$_{16}$ SAs, the 2PPE intensity drastically increases, particularly in the lower energy region due to the nonlinear optical response of Ta@Si$_{16}$ SAs (section 3.1.4). Furthermore, a new spectral feature appears at 6.2 eV in the final state energy. This photoemission signal originates from the conduction band electron at $E_F + 2.1$ eV photoexcited in the Ta@Si$_{16}$ SA film (section 3.2.2). In the low-energy cutoff region, the onset energy reveals the behaviors of the work function and shows coverage dependence; up to less than 1 ML, the cutoff energy shifts toward a lower energy, while it slightly increases at higher coverages.

3.1.2. Ta@Si$_{16}$ SA coverage dependence of the work function. It has been demonstrated that the p-type (alkaline-like) Ta@Si$_{16}$ SA is stably immobilized on the n-type C$_{60}$ substrate, which exhibits a large electron affinity.[65] This interaction results in charge transfer at the interface between Ta@Si$_{16}$ and C$_{60}$. Notably, the observed change in the work function in the low-coverage region (from sub-ML to several MLs) clearly reflects this interfacial charge transfer, leading to the formation of a surface dipole.

Fig. 2(b) shows the magnified 2PPE spectra of Fig. 2(a) in the low-energy cutoff regions on a logarithmic intensity scale. With Ta@Si$_{16}$ SA deposition up to less than 1 ML, the work function gradually decreases by approximately 0.3 eV from 4.7 to 4.4 eV, while it increases to about 4.5 eV at higher depo-

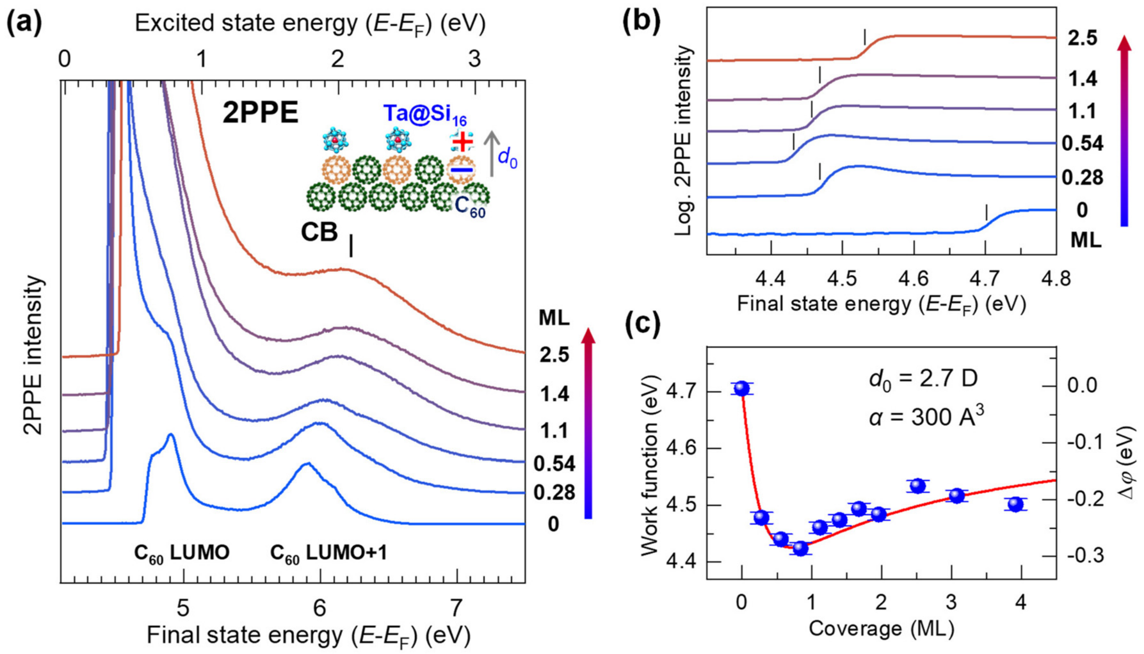

Fig. 2 (a) Coverage-dependent 2PPE spectra ($h\nu$ = 4.13 eV) of the Ta@Si$_{16}$ SA on C$_{60}$. The bottom and top axes represent the energies of the final state and the intermediately excited state with respect to the E_F, respectively. Before SA deposition, the C$_{60}$-derived LUMO and LUMO+1 levels are observed at E_F + 0.8 eV and E_F + 1.8 eV (see the top axis).[61] The 2PPE intensity is significantly enhanced by SA deposition, especially at the lower energy. The low-energy cutoff of the 2PPE spectra in the final state energy corresponds to the vacuum level (=E_F + work function). A peak at 6.2 eV in the final state energy is a conduction band (CB) structure of the SA film at E_F + 2.1 eV (top axis). (b) Magnified 2PPE spectra at the low-energy cut off region on a logarithmic intensity scale. The work function (marked by vertical bars) decreases by 0.3 eV at lower coverages of up to 1 ML, while it slightly increases at coverages greater than 1 ML. (c) The coverage-dependent work function attributable to the electron-donating p-type (alkaline-like) properties of the Ta@Si$_{16}$ SA, similar to alkaline atom deposition. The change in the work function, $\Delta\varphi$ (right axis), is fitted using a Topping model[66] with eqn (1), providing an adsorption-induced dipole moment, d_0, of 2.7 D.

sition amounts (>1 ML). More detailed work functions are plotted against the SA coverages, as shown in Fig. 2(c).

The characteristic change in the work function is closely associated with that of the well-studied adsorption behavior of alkaline atoms on metal or semiconductor substrates.[66] This can be explained by: (1) a surface dipole layer formed by electron-donating alkaline adatoms on the substrate lowering the work function, (2) the dipole layer being lifted by depolarization at coverages approaching 1 ML, and (3) the work function slightly recovering at multilayer coverages. Therefore, our experimental results indicate that an adsorption-induced dipole layer forms at the first layer of the p-type (alkaline-like) Ta@Si$_{16}$ SA film on C$_{60}$, driven by interfacial charge transfer (inset in Fig. 2(a)).

More quantitatively, the change in the work function, $\Delta\varphi$ (right axis in Fig. 2(c)), due to the formation of a surface dipole layer can be described by the Topping model[66] as:

$$\Delta\varphi = -{\varepsilon_0}^{-1} d_0 n_{\mathrm{ad}}\left(1+9\alpha' n_{\mathrm{ad}}^{\frac{3}{2}}\right), \tag{1}$$

where ε_0, d_0, n_{ad}, and α' are the permittivity in a vacuum, dipole moment, surface density, and mean polarizability, respectively. Assuming that each C$_{60}$ molecule faces a Ta@Si$_{16}$ SA at the interface, n_{ad} can be estimated as the surface density of C$_{60}$, 1.18 nm^{-1}.[67] The experimental result fits eqn (1) with d_0 = 2.7 D (1 D = 3.3 × 10^{-30} Cm) and α' = 300 Å^3. Note that the d_0 value is smaller than the calculated dipole moment for the free V@Si$_{16}$ (p-type SA)–Sc@Si$_{16}$ (n-type SA) heterodimer (d_0 = 7.6 D or 5.7 D depending on the calculation level).[68] This smaller d_0 value in a Ta@Si$_{16}$–C$_{60}$ complex shows a difference in electron distribution at the microscopic level; the negative charge may be inclined towards the Ta@Si$_{16}$ side of the C$_{60}$ layer in Ta@Si$_{16}$–C$_{60}$, while in the V@Si$_{16}$–Sc@Si$_{16}$ heterodimer, electron distributions are located at the central Sc metal.[69] Note that the α' value is evaluated for a Ta@Si$_{16}$–C$_{60}$ "complex" at the interface exhibiting the finite dipole moment (2.7 D). Although the fitting becomes unrealistic at thicknesses greater than 1 ML, it does not significantly impact the α' value fitting within the range of 100 < α' < 400. This coverage-dependent work function analysis concludes that the Ta@Si$_{16}$ SA provides negative charge to the adjacent C$_{60}$, forming an interfacial dipole layer due to its p-type (alkaline-like) nature based on one-electron excess against the 68-electron shell closure.[14,17,20,21]

3.1.3. Electronic excited state of Ta@Si$_{16}$ on C$_{60}$.

In the coverage-dependent 2PPE spectra of Ta@Si$_{16}$ SAs (Fig. 2(a)), a new peak at 6.2 eV appears in the final state energy after SA deposition at coverages greater than 1 ML. Since the SA coverage of 2.5 MLs (the highest SA amount in Fig. 2(a)) is sufficient to obscure the photoemission from the underlying C$_{60}$ (see also the 7 ML film in Fig. 7), the photoemission signal originates from the Ta@Si$_{16}$ SA film itself. In general, the 2PPE signal in the spectral feature must be attributed to the valence or conduction band electrons, as both bands can contribute to the 2PPE spectrum. By examining the UPS spectra of the thick Ta@Si$_{16}$ SA films (see Fig. 7), a much broader valence band structure is observed at the corresponding binding energy ($E_F - 2$ eV; $E_F + (6.2 - 2\ h\nu)$ eV). Therefore, the peak structure at 6.2 eV in the final state energy is attributable to an intermediately excited electron by one-photon absorption; *i.e.* the 2PPE peak is assignable to photoemission from the conduction band located at $E_F + 2.1$ eV ($E_F + (6.2 - 1\ h\nu)$ eV), as shown by the top axis in Fig. 2(a). The conduction band structures of the Ta@Si$_{16}$ layers are discussed in section 3.2.2, together with UPS and DFT calculations. Note that we have accurately measured the electronic structures of a pure Ta@Si$_{16}$ film without any oxidation or degradation, where 2PPE (and UPS) has a high surface sensitivity to oxidations at the topmost surface. In fact, the UPS and XPS spectra drastically change upon intentional oxygen exposure to the SA film (see ESI Fig. S2 and S3†), where both spectra become similar to that of an SiO$_2$ film[76] due to the oxidative reaction of the topmost Ta@Si$_{16}$ SA.

As shown in the 2PPE spectra of Ta@Si$_{16}$ SAs in the lower energy region (Fig. 2(a)), a dramatic enhancement of the 2PPE intensity is observed. Since the intensity enhancement is clearly recognizable even at sub-ML coverages, the 2PPE spectral feature does not merely reflect the density of states of the Ta@Si$_{16}$ film itself. A plausible explanation for the intensity enhancement in the 2PPE spectra is the nonlinear optical response (*e.g.* nonlinear scattering) of Ta@Si$_{16}$ SAs, where 2PPE sensitively responds to the generated near-field with the nonlinear optical response. In fact, no photoemission enhancement occurs in UPS using the a cw discharge lamp; the UPS intensity is rather suppressed by Ta@Si$_{16}$ deposition due to the large difference in the ionization cross-sections between the C 2p- and Si 3p-derived valence electrons.[70] Similar 2PPE enhancements have been reported in plasmonic silver nanoparticle/NC-deposited surfaces around their photoexcitation energies of localized surface plasmon resonance.[48,55] The present results show that the Si-based SA can serve as a sensitive probe of nonlinear optical phenomena at the surface and/or interface, demonstrating its capability as a photo-sensitizer as described in the next section.

3.1.4. Microscopy sensitizer of Ta@Si$_{16}$ for photoemission electron microscopy. As mentioned above, the photoemission signals with nonlinear excitation are strongly enhanced even by a small amount of Ta@Si$_{16}$ SA deposition. This enables the size-selective deposition of the Ta@Si$_{16}$ SA to act as a sensitizer for microscopic near-field imaging, *e.g.* plasmonic excitation. In this section, the sensitive nonlinear imaging and characterization of surface plasmon polaritons (SPPs) propagating at a metal/dielectric interface are demonstrated. In general, propagating SPPs are visualized by microscopic imaging of 2PPE using a PEEM (*i.e.* 2P-PEEM).[51–58] However, this powerful SPP imaging method is typically valid only for bare plasmonic metal structures that can photoemit with an SPP-exciting pump photon *via* two-photon and 2PPE processes. Lowering the work function by alkali-atom deposition is often required to extract photoelectrons under vacuum. In fact, almost no 2PPE signal is obtained for a C$_{60}$ (>10 ML) film prepared on a plasmonic Au substrate with SPP-exciting near-infrared (NIR; $h\nu = \sim 1.5$ eV) photons, even with the assistance of co-irradiating ultraviolet (UV; $h\nu = 4.5$ eV) photons. Therefore, it is principally difficult to visualize as is the SPPs by 2P-PEEM at a "buried" interface.[55]

To address this issue, Ta@Si$_{16}$ SAs deposited on a plasmonic C$_{60}$/Au system are useful for effectively converting the near-field generated by propagating SPPs into nonlinear photoemission. Fig. 3(a) and (b) show the two-color 2P-PEEM (NIR: $h\nu = 1.44$ eV and UV: $h\nu = 4.32$ eV) images of 10 ML C$_{60}$/Au decorated with (a) 0.1 ML and (b) 1 ML Ta@Si$_{16}$ SAs. Fringe patterns propagating from an intrinsic groove are observed in 2P-PEEM. Such characteristic fringe patterns in 2P-PEEM were first observed by Kubo *et al.*[71] for a silver thin film deposited on a mica substrate. The patterns result from the surface polarization beats formed by the interference between the electromagnetic fields induced by propagating SPPs and the remaining light. In the present 2P-PEEM, incident NIR photons form polarisation beats with SPP excitation at the C$_{60}$/Au interface, and the interference fringe patterns are imaged by 2P-PEEM, where nonlinear photoemission from the Ta@Si$_{16}$ SAs is induced simultaneously by illuminated UV photons,[48,54,55,72] as schematically illustrated in Fig. 3(c). We would like to reiterate that no imaging of the buried SPPs at the C$_{60}$/Au interface is available without decorating Ta@Si$_{16}$ SAs; Ta@Si$_{16}$ SAs play the role of sensitizers for the nonlinear photoelectron source accompanied by SPP propagation at the interface.

The lateral period of the beat patterns in 2P-PEEM ($\lambda_{\text{beat}} = 2\pi/k_{\text{beat}}$) sensitively reflects the physical properties of SPPs (Fig. 3(d)), which are largely perturbed by the overlayered dielectric films. In turn, SA-sensitized SPP imaging is a powerful method to characterize the SPPs propagating at the buried interface. The wave vector of SPPs, k_{spp}, excited by an incident photon ($h\nu = hc/\lambda_0 = hck_0/2\pi$, where c is the speed of light) at the dielectric/metal interface can be experimentally evaluated by $k_{\text{spp}} = k_{\text{beat}} + k_0$, which was found to be $7.49 \times 10^6\ \text{m}^{-1}$ at $h\nu = 1.44$ eV. On the other hand, k_{spp} can be simulated using an extended Drude model described by Kretschmann's equation:[73]

$$k_{\text{spp}} = k_0\sqrt{\frac{\varepsilon_{\text{m}}\varepsilon_{\text{vac}}}{\varepsilon_{\text{m}}+\varepsilon_{\text{vac}}}} + k_0\left(\frac{\varepsilon_{\text{d}}-\varepsilon_{\text{vac}}}{\varepsilon_{\text{d}}}\right)\left(\frac{\varepsilon'_{\text{m}}\varepsilon_{\text{vac}}}{\varepsilon'_{\text{m}}+\varepsilon_{\text{vac}}}\right)^2\left(\frac{\varepsilon_{\text{d}}-\varepsilon'_{\text{m}}}{\varepsilon_{\text{vac}}-\varepsilon'_{\text{m}}}\right) \times \left(-\varepsilon'_{\text{m}}\varepsilon_{\text{vac}}\right)^{-\frac{1}{2}}\left(\frac{2\pi t}{\lambda_0}\right), \tag{2}$$

where ε_{m} and ε_{d} are the dielectric constants of the metal and dielectric, respectively, and t is the thickness of the dielectric layer. The simulated k_{spp} values ($7.51 \times 10^6\ \text{m}^{-1}$ for $h\nu = 1.44$ eV) for the 10 ML C$_{60}$ thickness ($\varepsilon_{\text{d}} = 4.5$,[74] $h = 10$ nm (ref. 75))

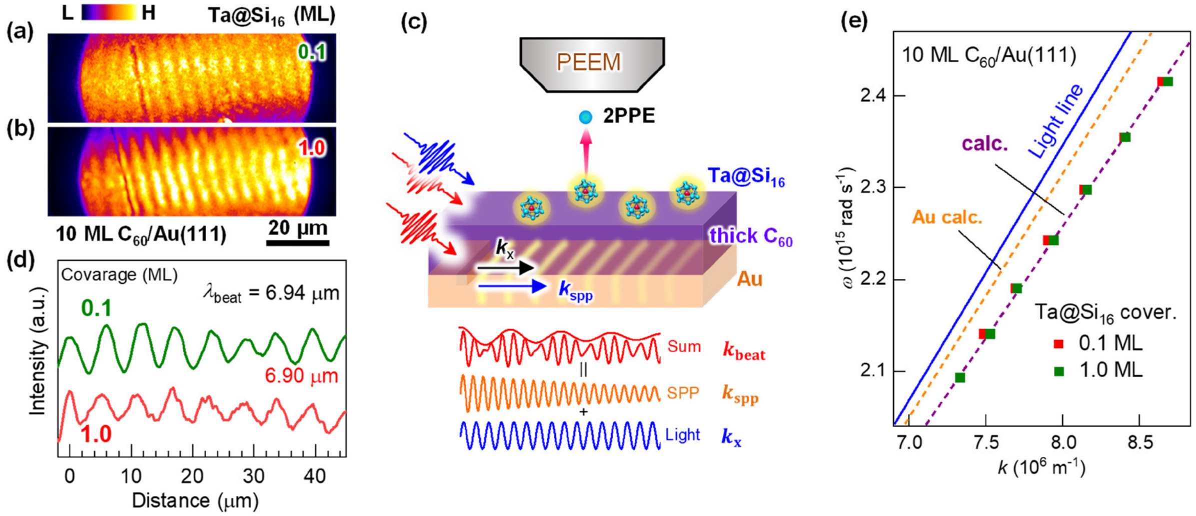

Fig. 3 (a and b) Two-color 2P-PEEM images (NIR; $h\nu$ = 1.44 eV and UV; $h\nu$ = 4.33 eV) of 10 ML C_{60}/Au(111) after Ta@Si_{16} deposition for (a) 0.1 ML and (b) 1 ML. (c) Schematic illustration of SA-sensitized SPP visualization by 2P-PEEM. (d) Horizontal intensity profiles of (a) and (b), showing that the internal SPP properties are negligibly modified by Ta@Si_{16} deposition of up to 1 ML. (e) SPP dispersion of 10 ML C_{60}/Au(111) sensitised by the Ta@Si_{16} SAs, which is evaluated from the $h\nu$ dependence (NIR; $h\nu$ = 1.41–1.54 eV) of λ_{beat}. The calculated SPP dispersions for Au and 10 ML C_{60}/Au are superimposed in (e).

consistently reproduce the experimental results of the present C_{60}/Au(111) system.

The fringe pattern due to SPP propagation becomes more obvious at the higher Ta@Si_{16} coverage of 1 ML (Fig. 3(b)). As seen in the vertical line profile along with the k_x (Fig. 3(d)), the λ_{beat} is mostly independent of the Ta@Si_{16} coverage at least up to 1 ML. The above results clearly demonstrate that the Ta@Si_{16} SAs have the capability to visualize the surface near-field penetrated from the buried plasmonic interface with negligible perturbations of their physical properties.

Furthermore, 2P-PEEM provides important information about the SPP properties at the interface, namely the SPP dispersion and velocities. These physical properties of SPPs at the buried interface have been challenging to evaluate experimentally. Fig. 3(e) shows the SPP dispersion (ω *versus* k_{spp}) evaluated by the λ_{beat} obtained from 2P-PEEM at various photon energies (NIR; $h\nu$ = 1.41–1.54 eV). The dispersion curve is in excellent agreement with the curve calculated using eqn (2). The phase and group velocities of SPPs can also be extracted from ω/k and $d\omega/dk$, which were found to be 0.96–0.98 c and 0.89 c, respectively.

To summarize the electronic characterization and plasmonic sensitization of Ta@Si_{16} SAs, the energy diagram and excitation schemes with UV-UV and UV-NIR photons are illustrated in Fig. 4. Irradiation with SPP-exciting NIR and UV photons alone cannot energetically extract photoelectrons from the C_{60} surface (process (2) in Fig. 4). However, upon decorating with Ta@Si_{16} SAs, 2PPE with NIR-UV photons becomes effective (process (4) in Fig. 4; see also ESI Fig. S4† for the two-color 2PPE spectra), and its lateral distribution reflects the SPP-induced near-field at the surface. Notably, the enhancement of nonlinear photo-

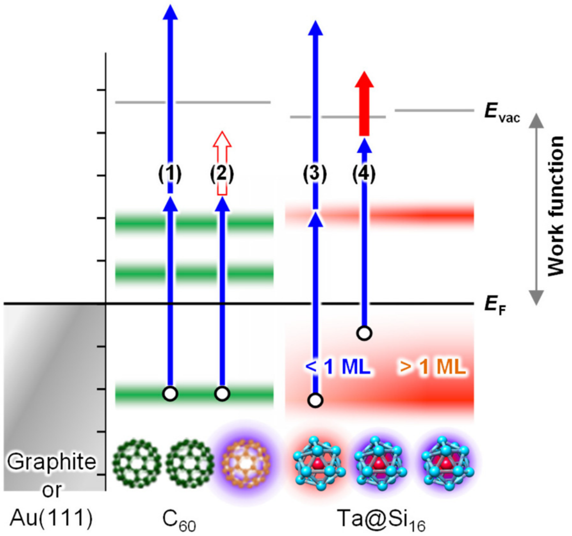

Fig. 4 Energy diagram of the Ta@Si_{16} SA film on a C_{60} substrate. The 2P-excitation schemes with UV and plasmon-exciting NIR photons are also indicated as blue and red arrows, respectively. UV–UV excitation (processes 1 and 3) produces a series of coverage-dependent 2PPE spectra of the Ta@Si_{16} SA on a C_{60} substrate (sections 3.1.1 and 3.1.3). The work function reaches a minimum at around 1 ML coverage of the Ta@Si_{16} SA due to charge transfer interactions with the topmost C_{60} (section 3.1.2). To visualize propagating SPPs at the buried C_{60}/Au(111) interface using 2P-PEEM (section 3.1.4), sufficient photoemission from the topmost surface is necessary. Without the Ta@Si_{16} SA, no photoemission occurs under UV–NIR excitation (process 2), while by decorating with the Ta@Si_{16} SA, UV–NIR excitation (process 4) results in sufficient photoemission, with the intensity enhanced by the SPP-induced near-field.

emission from the Ta@Si$_{16}$ SAs offers additional significant physical insights from the perspective of silicon plasmonics, where pure Si nanoparticles show no plasmonic response in the NIR or visible regions. In fact, the Ta@Si$_{16}$ film shows a density of states just below the E_F level (see Fig. 7), indicating the presence of free electrons capable of oscillating with an external electromagnetic field, *i.e.*, localized surface plasmons. These optical and plasmonic responses of such a "metal-doped Si nanoparticle" represent an exciting frontier that will be explored in the near future.

3.2. Electronic characterization of Ta@Si$_{16}$ SA thick films

3.2.1. X-ray photoelectron spectroscopy and plasmonic responses of the Ta@Si$_{16}$ thick film. To investigate the electronic properties of the thick Ta@Si$_{16}$ SA layers on a C$_{60}$ substrate, their XPS spectra were recorded at (a) Si 2p and (b) Ta 4f core levels for the thin (0.9 ML) and thick (7 ML) films of the Ta@Si$_{16}$ SA, as shown in Fig. 5. Detailed coverage-dependent XPS spectra are shown in ESI Fig. S1.† The intensities of Si 2p and Ta 4f core levels are consistent with the atomic composition ratio of 1 : 16 for Ta@Si$_{16}$ SAs.[27,28] Furthermore, the XPS peak profiles of Si 2p and Ta 4f are mostly reproduced by considering uniform chemical components within the instrumental peak broadening (1.12 eV FWHM), indicating that the Ta@Si$_{16}$ SA is deposited on the C$_{60}$ substrate while preserving its caged structure through favorable charge transfer interaction, forming a Ta@Si$_{16}$–C$_{60}$ complex (see section 3.1.2).[28] In addition, the coverage dependence of the C 1s peak shows a red shift by Ta@Si$_{16}$ SA deposition up to the full coverage (1 ML). In fact, when a gold (Au) (111) single crystal is used as a substrate, the Si 2p core level shows multiple chemical components, caused by significant distortion of the SAs on the metal substrate (see ESI Fig. S5†).

For thick films, the XPS peak width of Si 2p becomes narrower compared to thin films, particularly with reduced intensity at the higher binding energy side. This peak narrowing results in an apparent peak shift (0.2 eV) toward a lower binding energy. Since the chemical state of the central Ta atom remains almost unchanged as Ta^{1+} (22.5 eV)[28] regardless of the thickness, the spectral change in Si 2p indicates that the surrounding 16 Si atoms uniformly share a negative charge to compensate the overall charge of the Ta@Si$_{16}$ SA, making it neutral in the multilayered film, *i.e.* Ta^{1+}(Si$_{16}$)$^{1-}$. The charge states of the Ta@Si$_{16}$ SA at 1 ML and in the multilayer films are schematically illustrated in the inset of Fig. 5.

When bare Ta@Si$_{16}$ SAs accumulate and assemble into a multilayer, the inter-SA interactions should be induced by mixing the wave function with neighboring molecules, potentially leading to phenomena such as electric conduction[43,44] or charge separation. Interestingly, these inter-SA interactions are evidently resolved by XPS in a wider energy scan, characterized as plasmonic responses of the Ta@Si$_{16}$ SA layers. Fig. 6 shows the wide-range XPS spectra of the thin (0.6 ML) and thick (7 ML) Ta@Si$_{16}$ films on the C$_{60}$ substrate. Peaks at 117.2 eV and 41.6 eV appear in the thick film, where the energy separations from the main Si 2p and Ta 4f peaks are the same. The satellite peaks observed at the higher binding energies from the main core level peaks are associated with the energy loss of photoelectron kinetic energy due to plasmon excitation in the Ta@Si$_{16}$ SA film.[76–81] This plasmon excitation results from the collective oscillations of valence electrons, indicating the formation of an inter-SA chemical network between the bare Ta@Si$_{16}$ SAs.

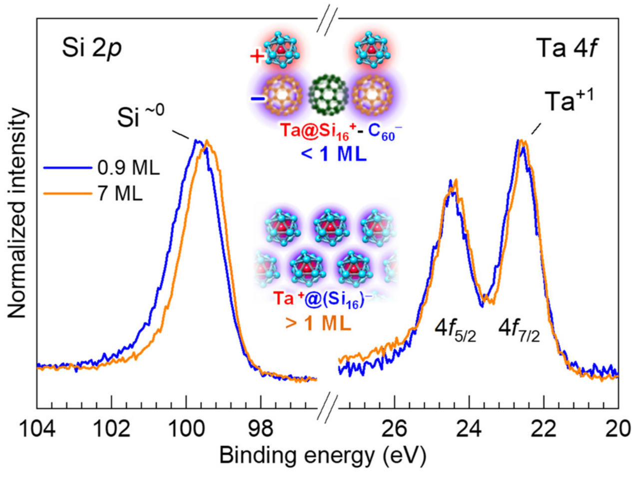

Fig. 5 Normalized XPS spectra of the thin (0.9 ML) and thick (7 ML) Ta@Si$_{16}$ SA films on a C$_{60}$ substrate. For the thick films, the Si 2p peak becomes sharper and shifts toward a lower binding energy, while the Ta 4f peak remained unchanged, corresponding to the Ta^{1+} charge state. This result indicates that the positive charge of Ta compensates for the negatively charged Si$_{16}$ cage, characterizing the Ta@Si$_{16}$ SA as neutral overall.

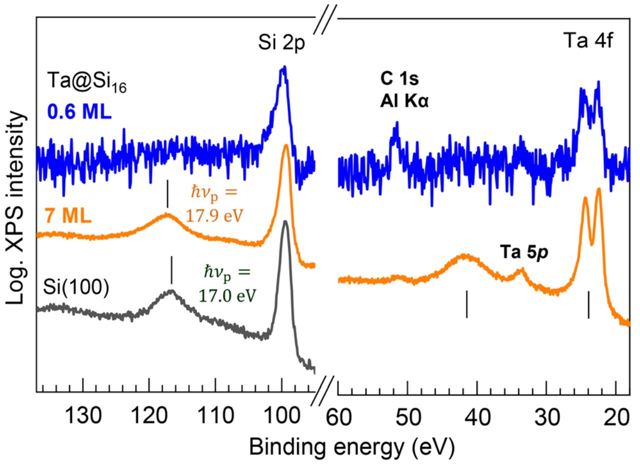

Fig. 6 Wide-scan XPS spectra for the thin (0.6 ML) and thick (7 ML) films of the Ta@Si$_{16}$ SA on C$_{60}$. In the thick film, satellite peaks are observed at the higher energy sides of the main Si 2p and Ta 4f peaks, exhibiting a common energy separation of 17.9 eV. These satellite peaks originate from the energy loss of photoelectrons due to plasmonic excitation in the Ta@Si$_{16}$ film. The plasma frequency ($h\nu_p$) is slightly higher than that observed for a clean Si(100) single crystal ($h\nu_p$ = 17.0 eV, bottom spectrum).[76]

The energy of plasmon energy loss, $h\nu_p$ = 17.9 eV, is slightly higher than that of bulk Si ($h\nu_p$ = 17.0 eV, see the bottom in Fig. 6).[76] It is known that the $h\nu_p$ changes with doping and quantum confinement, as reported in the literature when observing with XPS or electron energy loss spectroscopy (EELS) in Si-based systems.[77–81] In single Si nanocrystals with >2 nm diameter prepared from silane gas plasma,[77] the quantum confinement effect generally induces a blue shift of $h\nu_p$ (~1 eV in the smallest nanocrystals) because of the enlargement of the band gap. However, the quantum confinement effect can be excluded in the present system of the thick SA film, as no plasmon-induced energy loss peak is observable in the thin film (0.6 ML); the individual size of the Ta@Si$_{16}$ SA is too small to have the plasma oscillations of their valence electrons. Therefore, the blue shift of the $h\nu_p$ in the Ta@Si$_{16}$ film is considered to result from the effect of Ta doping in the Si cage (*i.e.* the doping effect[81]), although it is difficult to separately discuss the doping effects from many other possibilities (*e.g.* crystallinity, electronic structure, *etc.*). Note that a slight blue shift (0.3 eV) has been observed for multilayered Si$_n$ NCs on the substrate.[79]

3.2.2. **Ultraviolet photoelectron spectroscopy for the Ta@Si$_{16}$ thick film; electronic excitation.** Fig. 7 shows the UPS (left) and 2PPE (right) spectra of the 7 ML SA films, reflecting the valence and conduction band structures of the Ta@Si$_{16}$ layers. At this thickness, the contribution of the underlying substrate (C$_{60}$) in the UPS/2PPE spectra is negligible (see the coverage-dependent UPS/2PPE, ESI Fig. S6† (UPS) and Fig. 2 (2PPE)). In both spectra, appropriate smooth backgrounds due to secondary electrons were subtracted from the raw data to clearly show the electronic structures (see ESI Fig. S7† for the raw data). The higher energy onset of the UPS spectrum corresponds to the E_F, where the energy of E_F was carefully determined using a standard gold sample. The observed gapless valence electronic structure of the SA film is consistent with the ohmic electric conduction for the M@Si$_{16}$ (M = V, Nb, and Ta) films.[42,43]

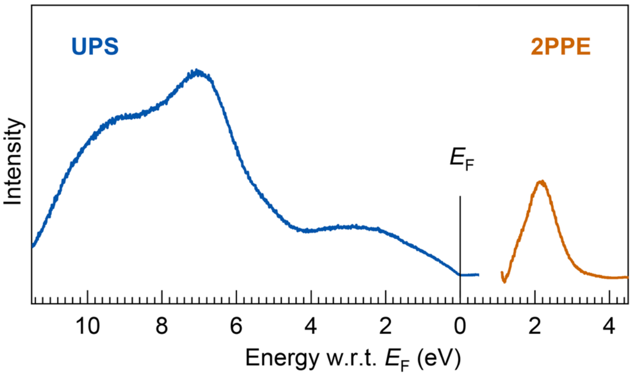

Fig. 7 (bottom) UPS and 2PPE spectra of a thick Ta@Si$_{16}$ SA film (7 MLs). The energy onset at E_F in the UPS spectrum indicates the ohmic electronic conduction of the Ta@Si$_{16}$ SA film. The broad valence and conduction band features, E_F − 2.6 eV, −7.0 eV, and −9.6 eV in UPS and E_F + 2.1 eV in 2PPE, are observed. The experimental results are compared with DFT calculations for the geometric isomer of neutral species and cations, as shown ESI Fig. S8.†

The electronic structures in the UPS spectrum exhibit broad features, implying a few major components such as those at binding energies of E_F − 2.6, −7.0, and −9.6 eV, while the conduction band feature is also resolved at E_F + 2.1 eV, as shown in Fig. 2(a). These broad electronic features might be due to inter-SA interactions between the non-ligated Si caged SAs, providing the plasmon-loss peaks in the XPS spectrum, as shown in Fig. 6. Note that we carefully evaluated the electronic states of the Ta@Si$_{16}$ SA film using UPS (and 2PPE) that are generally sensitive to oxidation or degradation of the topmost surface. Indeed, as evidenced by the drastic change in the UPS spectrum when the SA film is exposed to oxygen molecules (see ESI Fig. S3†), the resulting UPS spectrum closely resembles that of a thermally oxidized Si substrate.[82]

Importantly, the electronic structures are composed of more than 20 electronic states rather than a few broadened electronic states; the electronic states for a few geometric isomers of the free Ta@Si$_{16}$ neutral species and cations are calculated through DFT calculations (see ESI Note S2†). The comparison between the experimental and theoretical results is shown in ESI Fig. S8.† Although it is not straightforward to correlate the electronic structures in the assembled layers with the electronic states of isolated species obtained from the Kohn–Sham orbitals and eigenvalues from the DFT calculations,[83,84] the calculations suggest that more than 20 electronic states are involved in the region. The calculated electronic states for a few geometric isomers are shown in ESI Fig. S9 and Tables S1 (cation) and S2 (neutral).† While the Kohn–Sham orbitals and orbital energies cannot exactly reproduce the electronic transitions, the comparison gives a rough picture of the electronic structures, breaking down the broadened electronic features in the condensed phase through inter-SA interactions. This also serves as a good target for extensive calculations of the electronic states using Hartree–Fock-based calculations.

4. Conclusions

To conclude, we have precisely fabricated a Ta@Si$_{16}$ SA film with mass-selective deposition onto a C$_{60}$ substrate. The work function decreases at the initial deposition of the SA (<1 ML) due to the formation of a dipole moment at the SA–substrate interface. Under the irradiation of a femtosecond laser, the photoemission is drastically enhanced because of the distinct nonlinear optical responses of Ta@Si$_{16}$ SAs, where the intense photoemission signal enables the visualization of the interfacial near-field due to plasmonic excitation. From XPS analysis, the charge state of the Ta@Si$_{16}$ SA in the thick film is characterized as Ta$^+$@(Si$_{16}$)$^-$, making neutral the Ta@Si$_{16}$ SAs as a whole. The UPS/2PPE spectra show the valence and conduction electronic structures of Ta@Si$_{16}$ SA films revealing broadening effects due to inter-SA interactions. The valence and conduction band features are in agreement with DFT calculations, originating from the superatomic nature. The electronic and optical characterization studies of the well-controlled SA films will facilitate the emergence of an era utilizing the novel functionalities of SA-assembled systems.

Author contributions

MS, TO, and TK conducted the photoelectron spectroscopy measurements of the SA films. MS and KY acquired the 2P-PEEM images of the SA-decorated plasmonic sample. HT, TI, and TM calculated the electronic structures of the SAs. MS and AN contributed to the writing processes. AN supervised the overall project.

Data availability

The data supporting this article have been included as part of the ESI.†

Conflicts of interest

There are no conflicts to declare.

Acknowledgements

This work was partly supported by the program of Exploratory Research for Advanced Technology (ERATO) in the Japan Science and Technology Agency (JST) entitled the “Nakajima Designer Nanocluster Assembly Project”, JSPS KAKENHI of Grant-in-Aid for Scientific Research (A) No. 19H00890, Scientific Research (B) No. 23H01939, 24K01277, and 24K01442 and Scientific Research (C) No. 18K04942, and Transformative Research Areas (A) “Hyper–Ordered Structures Science” No. 21H05573. A. N. is grateful for support from the Alexander von Humboldt Foundation.

References

1 T. Bernhardt, U. Heiz and U. Landman, *Chemical and Catalytic Properties of Size-Selected Free and Supported Clusters*, Springer, Berlin, Heidelberg, 2007.
2 A. W. Castleman Jr., *J. Phys. Chem. Lett.*, 2011, **2**, 1062–1069.
3 P. Jena, *J. Phys. Chem. Lett.*, 2013, **4**, 1432–1442.
4 D. A. Tomalia and S. N. Khanna, *Chem. Rev.*, 2016, **116**, 2705–2774.
5 Z. Luo, A. W. Castleman Jr. and S. N. Khanna, *Chem. Rev.*, 2016, **116**, 14456–14492.
6 A. C. Reber and S. N. Khanna, *Acc. Chem. Res.*, 2017, **50**, 255–263.
7 P. Jena and Q. Sun, *Chem. Rev.*, 2018, **118**, 5755–5870.
8 P. Ferrari, J. Vanbuel, E. Janssens and P. Lievens, *Acc. Chem. Res.*, 2018, **51**, 3174–3182.
9 H. W. Kroto, J. R. Heath, S. C. O'Brien, R. F. Curl and R. E. Smalley, *Nature*, 1985, **318**, 162–163.
10 D. E. Bergeron, A. W. Castleman Jr., T. Morisato and S. N. Khanna, *Science*, 2004, **304**, 84–87.
11 J. U. Reveles, S. N. Khanna, P. J. Roach and A. W. Castleman Jr., *Proc. Natl. Acad. Sci. U. S. A.*, 2006, **103**, 18405–18410.
12 A. C. Reber, S. N. Khanna and A. W. Castleman Jr., *J. Am. Chem. Soc.*, 2007, **129**, 10189–10194.
13 A. Nakajima, T. Kishi, T. Sugioka and K. Kaya, *Chem. Phys. Lett.*, 1991, **187**, 239–244.
14 K. Koyasu, M. Akutsu, M. Mitsui and A. Nakajima, *J. Am. Chem. Soc.*, 2005, **127**, 4998–4999.
15 H. Hiura, T. Miyazaki and T. Kanayama, *Phys. Rev. Lett.*, 2001, **86**, 1733–1736.
16 M. B. Torres, E. M. Fernández and L. C. Balbás, *Phys. Rev. B: Condens. Matter Mater. Phys.*, 2007, **75**, 205425.
17 K. Koyasu, J. Atobe, M. Akutsu, M. Mitsui and A. Nakajima, *J. Phys. Chem. A*, 2007, **111**, 42–49.
18 J. T. Lau, K. Hirsch, Ph. Klar, A. Langenberg, F. Lonfink, R. Richter, J. Rittman, M. Vogel, V. Zamudio-Bayer, T. Möller and B. von Issendorff, *Phys. Rev. A*, 2009, **79**, 053201.
19 J. T. Lau, M. Vogel, A. Langenberg, K. Hirsch, J. Rittmann, V. Zamudio-Bayer, T. Möller and B. von Issendorff, *J. Chem. Phys.*, 2011, **134**, 041102.
20 J. Atobe, K. Koyasu, S. Furuse and A. Nakajima, *Phys. Chem. Chem. Phys.*, 2012, **14**, 9403–9410.
21 A. Sen and S. Sen, *J. Phys. Chem. C*, 2017, **121**, 28490–28497.
22 Y. Negishi, K. Nobusada and T. Tsukuda, *J. Am. Chem. Soc.*, 2005, **127**, 5261–5270.
23 Y. Negishi, H. Tsunoyama, M. Suzuki, N. Kawamura, M. M. Matsushita, K. Maruyama, T. Sugawara, T. Yokoyama and T. Tsukuda, *J. Am. Chem. Soc.*, 2006, **128**, 12034–12035.
24 H. Häkkinen, *Chem. Soc. Rev.*, 2008, **37**, 1847–1859.
25 T. Laaksonen, V. Ruiz, P. Liljeroth and B. M. Quinn, *Chem. Soc. Rev.*, 2008, **37**, 1836–1846.
26 R. Jin, *Nanoscale*, 2010, **2**, 343–362.
27 M. Shibuta, T. Ohta, M. Nakaya, H. Tsunoyama, T. Eguchi and A. Nakajima, *J. Am. Chem. Soc.*, 2015, **137**, 14015–14018.
28 T. Ohta, M. Shibuta, H. Tsunoyama, T. Eguchi and A. Nakajima, *J. Phys. Chem. C*, 2016, **120**, 15265–15271.
29 H. Tsunoyama, H. Akatsuka, M. Shibuta, T. Iwasa, Y. Mizuhata, N. Tokitoh and A. Nakajima, *J. Phys. Chem. C*, 2017, **121**, 20507–20516.
30 H. Tsunoyama, M. Shibuta, M. Nakaya, T. Eguchi and A. Nakajima, *Acc. Chem. Res.*, 2018, **51**, 1735–1745.
31 M. Shibuta, T. Kamoshida, T. Ohta, H. Tsunoyama and A. Nakajima, *Commun. Chem.*, 2018, **1**, 50.
32 M. Shibuta, T. Niikura, T. Kamoshida, H. Tsunoyama and A. Nakajima, *Phys. Chem. Chem. Phys.*, 2018, **20**, 26273–26279.
33 T. Kamoshida, M. Shibuta, T. Ohta, T. Eguchi and A. Nakajima, *J. Phys. Chem. C*, 2022, **126**, 10889–10899.
34 M. Shibuta, T. Inoue, T. Kamoshida, T. Eguchi and A. Nakajima, *Nat. Commun.*, 2022, **13**, 1336.
35 T. Inoue, M. Hatanaka and A. Nakajima, *J. Am. Chem. Soc.*, 2023, **145**, 23088.

36 K. Terasaka, T. Kamoshida, T. Ichikawa, T. Yokoyama, M. Shibuta and A. Nakajima, *J. Am. Chem. Soc.*, 2024, **146**, 9605–9613.

37 S. N. Khanna and P. Jena, *Phys. Rev. Lett.*, 1992, **69**, 1664–1667.

38 S. N. Khanna and P. Jena, *Phys. Rev. B: Condens. Matter Mater. Phys.*, 1995, **51**, 13705–13716.

39 M. Nakaya, T. Iwasa, H. Tsunoyama, T. Eguchi and A. Nakajima, *Nanoscale*, 2014, **6**, 14702–14707.

40 M. Nakaya, T. Iwasa, H. Tsunoyama, T. Eguchi and A. Nakajima, *J. Phys. Chem. C*, 2015, **119**, 10962–10968.

41 T. Inoue, T. Ina, H. Masai, N. Kondo, F. Matsui, T. Kinoshita and A. Nakajima, *J. Phys. Chem. Lett.*, 2024, **15**, 5376–5381.

42 M. Shibuta, R. Takano and A. Nakajima, *J. Phys. Chem. C*, 2020, **124**, 28108–28115.

43 T. Yokoyama, T. Chiba, N. Hirata, M. Shibuta and A. Nakajima, *J. Phys. Chem. C*, 2021, **125**, 18420–18428.

44 T. Yokoyama and A. Nakajima, *Phys. Chem. Chem. Phys.*, 2023, **25**, 9738–9752.

45 H. Petek and S. Ogawa, *Prog. Surf. Sci.*, 1997, **56**, 239–310.

46 J. Güdde and U. Höfer, *Prog. Surf. Sci.*, 2005, **80**, 49–91.

47 T. Yamada and T. Munakata, *Prog. Surf. Sci.*, 2018, **93**, 108–130.

48 M. Shibuta and A. Nakajima, *J. Phys. Chem. Lett.*, 2023, **14**, 3285–3295.

49 M. Bauer, A. Marienfeld and M. Aeschlimann, *Prog. Surf. Sci.*, 2015, **90**, 319–376.

50 C. H. Zhang, H. Tsunoyama, H. Akatsuka, H. Sekiya, T. Nagase and A. Nakajima, *J. Phys. Chem. A*, 2013, **117**, 10211–10217.

51 M. Aeschlimann, T. Brixner, A. Fischer, C. Kramer, P. Melchior, W. Pfeiffer, C. Schneider, C. Strüber, P. Tuchscherer and D. V. Voronine, *Science*, 2011, **333**, 1723–1726.

52 C. Lemke, T. Leißner, A. Evlyukhin, J. W. Radke, A. Klick, J. Fiutowski, J. Kjelstrup-Hansen, H.-G. Rubahn, B. N. Chichkov, C. Reinhardt and M. Bauer, *Nano Lett.*, 2014, **14**, 2431–2435.

53 C. Lemke, T. Leißner, A. Klick, J. Fiutowski, J. W. Radke, M. Thomaschewski, J. Kjelstrup-Hansen, H.-G. Rubahn and M. Bauer, *Appl. Phys. B: Lasers Opt.*, 2014, **116**, 585–591.

54 K. Yamagiwa, M. Shibuta and A. Nakajima, *Phys. Chem. Chem. Phys.*, 2017, **19**, 13455–13461.

55 K. Yamagiwa, M. Shibuta and A. Nakajima, *ACS Nano*, 2020, **14**, 2044–2052.

56 M. Dąbrowski, Y. Dai and H. Petek, *Chem. Rev.*, 2020, **120**, 6247–6287.

57 M. Großmann, M. Black, J. Jaruschewski, A. Klick, T. Leißner, J. Fiutowski, H.-G. Rubahn and M. Bauer, *Plasmonics*, 2021, **16**, 737–746.

58 M. Hartelt, P. N. Terekhin, T. Eul, A.-K. Mahro, B. Frisch, E. Prinz, B. Rethfeld, B. Stadtmüller and M. Aeschlimann, *ACS Nano*, 2021, **15**, 19559–19569.

59 T. Ohta, M. Shibuta, H. Tsunoyama, Y. Negishi, T. Eguchi and A. Nakajima, *J. Phys. Chem. C*, 2013, **117**, 3674–3679.

60 M. Shibuta, K. Yamamoto, T. Ohta, T. Inoue, K. Mizoguchi, M. Nakaya, T. Eguchi and A. Nakajima, *ACS Nano*, 2021, **15**, 1199–1209.

61 M. Shibuta, K. Yamamoto, T. Ohta, M. Nakaya, T. Eguchi and A. Nakajima, *Sci. Rep.*, 2016, **6**, 35853.

62 M. Shibuta, N. Hirata, T. Eguchi and A. Nakajima, *ACS Nano*, 2017, **11**, 4307–4314.

63 M. Shibuta, K. Yamagiwa, T. Eguchi and A. Nakajima, *Appl. Phys. Lett.*, 2016, **109**, 203111.

64 M. Shibuta and A. Nakajima, *Nanoscale*, 2024, **16**, 12397–12405.

65 D. L. Huang, P. D. Dau, H. T. Liu and L. S. Wang, *J. Chem. Phys.*, 2014, **140**, 224315.

66 H. Lüth, *Solid Surfaces, Interfaces and Thin Films*, Springer, Berlin, 2001.

67 M. Jung, D. Shin, S.-D. Sohn, S.-Y. Kwon, N. Park and H.-J. Shin, *Nanoscale*, 2014, **6**, 11835.

68 T. Iwasa and A. Nakajima, *J. Phys. Chem. C*, 2012, **116**, 14071–14077.

69 M. Chen, I. P. Batra and C. R. Brundle, *J. Vac. Sci. Technol.*, 1979, **16**, 1216–1220.

70 J. C. Green and P. Decleva, *Coord. Chem. Rev.*, 2005, **249**, 209–228.

71 A. Kubo, N. Pontius and H. Petek, *Nano Lett.*, 2007, **7**, 470–475.

72 M. Shibuta, T. Eguchi and A. Nakajima, *Plasmonics*, 2013, **8**, 1411–1415.

73 E. Kretschmann, *Z. Phys.*, 1971, **241**, 313–324.

74 S. L. Ren, Y. Wang, A. M. Rao, E. McRae, J. M. Holden, T. Hager, K. Wang, W.-T. Lee, H. F. Ni, J. Selegue and P. C. Eklund, *Appl. Phys. Lett.*, 1991, **59**, 2678–2680.

75 W. Krätschmer, L. D. Lamb, K. Fostiropoulos and D. R. Huffman, *Nature*, 1990, **347**, 354–358.

76 T. L. Barr, *Modern ESCA, The Principles and Practice of X-Ray Photo-electron Spectroscopy*, CRC, Boca Raton, 1994.

77 M. Mitome, Y. Yamazaki, H. Takagi and T. Nakagiri, *J. Appl. Phys.*, 1992, **72**, 812–814.

78 N. Dibiase, G. Gabetta, A. Lumachi, M. Scagliotti and F. Parmigiani, *Appl. Phys. Lett.*, 1995, **67**, 2491–2493.

79 P. Mélinon, P. Kéghélian, B. Prével, A. Perez, G. Guiraud, J. LeBrusq, J. Lermé, M. Pellarin and M. Broyer, *J. Chem. Phys.*, 1997, **107**, 10278–10287.

80 N. Mannella, G. Gabetta and F. Parmigiani, *Appl. Phys. Lett.*, 2001, **79**, 4432–4434.

81 M. Duchamp, C. B. Boothroyd, M. S. Moreno, B. B. van Aken, W. J. Soppe and R. E. Dunin-Borkowski, *J. Appl. Phys.*, 2013, **113**, 093513.

82 A. J. Schell-Sorokin and J. E. Demuth, *Surf. Sci.*, 1985, **157**, 273–296.

83 R. Stowasser and R. Hoffmann, *J. Am. Chem. Soc.*, 1999, **121**, 3414–3420.

84 R. van Meer, O. V. Gritsenko and E. J. Baerends, *J. Chem. Theory Comput.*, 2014, **10**, 4432–4441.